PHYSICAL REVIEW B **105**, 205201 (2022)

Out-of-plane thermoelectric performance for *p*-doped GeSe

Anderson S. Chaves,[1,2] Daniel T. Larson,[3] Efthimios Kaxiras,[3,2] and Alex Antonelli[4]
[1]*Gleb Wataghin Institute of Physics, University of Campinas, P.O. Box 13083-859, Campinas, SP, Brazil*
[2]*John A. Paulson School of Engineering and Applied Sciences, Harvard University, Cambridge, Massachusetts 02138, USA*
[3]*Department of Physics, Harvard University, Cambridge, Massachusetts 02138, USA*
[4]*Gleb Wataghin Institute of Physics and Center for Computing in Engineering & Sciences,*
University of Campinas, P.O. Box 13083-859, Campinas, SP, Brazil

(Received 15 February 2022; accepted 25 April 2022; published 6 May 2022)

The record-breaking thermoelectric performance of tin selenide (SnSe) has motivated the investigation of analog compounds with the same structure. A promising candidate that emerged recently is germanium selenide (GeSe). Here, using extensive first-principles calculations of the hole-phonon and hole-impurity scattering, we investigate the thermoelectric transport properties of the orthorhombic phase of *p*-doped GeSe. We predict outstanding thermoelectric performance for GeSe over a broad range of temperatures due to its high Seebeck coefficients, extremely low Lorenz numbers, ultralow total thermal conductivity, and relatively large band gap. In particular, the out-of-plane direction in GeSe presents equivalent or even higher performance than SnSe for temperatures above 500 K. By extending the analysis to 900 K, we obtained an ultrahigh value for the thermoelectric figure of merit ($zT = 3.2$) at the optimal hole density of $4 \times 10^{19}\,\mathrm{cm}^{-3}$. Our work provides strong motivation for continued experimental work focusing on improving the GeSe doping efficiency in order to achieve this optimal hole density.

DOI: 10.1103/PhysRevB.105.205201

I. INTRODUCTION

High-efficiency thermoelectric (TE) materials have been systematically and comprehensively investigated during the past several decades, mainly due to their capability of functioning as all-solid-state modules for distributed spot-size refrigeration [1,2] or electric power generation from waste heat [3,4]. The key quantity to evaluate the efficiency of TE energy conversion is the dimensionless figure of merit, $zT = \sigma S^2 T/\kappa_{\mathrm{tot}}$, where σ, S, and T stand for the electrical conductivity, the Seebeck coefficient, and the absolute temperature, and $\kappa_{\mathrm{tot}} = \kappa_{\mathrm{latt}} + \kappa_{\mathrm{h}}$ is the total thermal conductivity, comprised of lattice and electronic carrier contributions, respectively. Numerous TE materials have been discovered, and a few of them even have zT values between 2 and 3 [5–15]. However, even those high-zT materials do not have sufficient efficiency to be largely employed by industry [3,4,16]. Indeed, it has been argued that materials with $zT > 3$ would represent a highly attractive prospect for applications, allowing TE refrigerators to compete with traditional compressor-based refrigerators [1,17]. Such ultrahigh zT values have not been measured in bulk materials until very recently [18]. Thus, TE materials have so far only found niche applications where reliability is of higher priority than efficiency.

The figure of merit, zT, can be enhanced either by increasing the power factor ($\mathrm{PF} = \sigma S^2$) or reducing the thermal conductivity, κ_{tot}. Ultimately, the main goal is to find TE materials that satisfy both of these conditions simultaneously, which is a challenge since the properties involved are interdependent. The maximization of PF relies on band-structure engineering [19–21] such as increasing band degeneracy through convergence of bands [22,23] or taking advantage of band-structure anisotropy [24] and nonparabolicity [25]. On the other hand, the main strategies to minimize κ_{tot} include identifying materials with intrinsically low κ_{latt} [26], minimizing the electronic carrier contribution, κ_{h}, through the minimization of the Lorenz function [27,28], or by alloying or nanostructuring procedures [22,29–32]. Despite the challenges, impressive achievements have been obtained on the basis of such strategies [4,12,33–38].

The record-breaking TE performance of SnSe [13–15] has motivated the investigation of analog IV-VI compounds with the same puckered layer structure in order to ascertain whether such systems also possess inherently low κ_{latt} and high zT. A promising candidate is germanium selenide (GeSe), which, like SnSe, crystallizes in the orthorhombic GeS-type structure shown in Fig. 1, with a space group of D_{2h}^{16} (*Pnma*) [39,40].

Additional advantages that make GeSe very attractive for large applications in thermoelectrics and photovoltaics include chemical stability, earth-abundance, environmental compatibility, and low toxicity (no lead) [41–45]. Recently, theoretical work by Ding *et al.* [46] put forward the possibility of achieving large S and PF values by proper *p*- or *n*-type doping of GeSe. Due to low thermal conductivity and multiband effects, Hao *et al.* [47] predicted an ultrahigh peak zT value of 2.5 along the in-plane (*b*-axis) direction of the orthorhombic phase of GeSe with a hole density of $6.5 \times 10^{19}\,\mathrm{cm}^{-3}$ at 800 K. If this could be realized, it would outperform *p*-doped SnSe. Though highly suggestive, that prediction used the same values for relaxation times and carrier densities as those

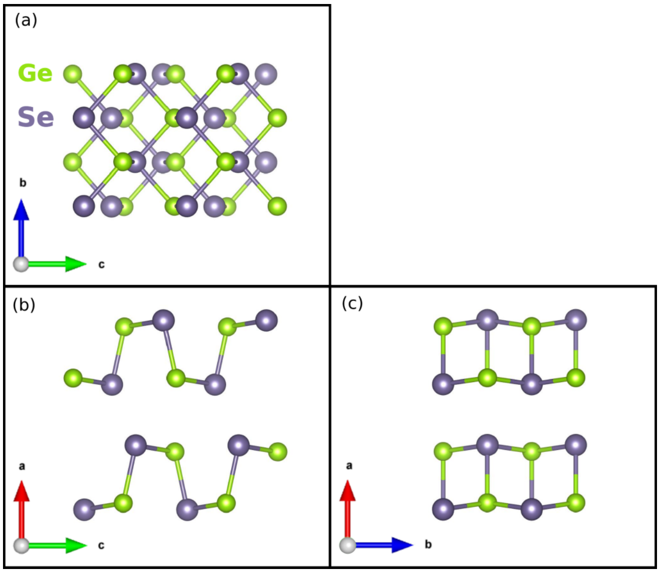

FIG. 1. Crystal structure of *Pnma* GeSe with views along each crystallographic direction: (a) perpendicular to the layer plane, (b), (c) along the layer planes. Green and gray spheres represent Ge and Se, respectively.

reported for p-doped SnSe. Despite the great potential of the orthorhombic phase of GeSe for TE applications, there are still relatively few published experimental results [48].

In the present work, we examine the thermoelectric performance of p-doped GeSe and SnSe within the Boltzmann transport equation (BTE) formalism by explicitly calculating relaxation times due to hole-phonon (h-p) and hole-impurity couplings using a comprehensive first-principles approach. In particular, the hole-phonon coupling was calculated by using the dual interpolation scheme [49] of the density functional theory (DFT) band structure [50,51]. The phonon dispersion and h-p matrix elements were determined by density functional perturbation theory (DFPT) [52]. The carrier density for the different axes was derived from the record-breaking transport data measured in p-doped SnSe [14]. The calculated temperature- and energy-dependent relaxation times allow for a deeper understanding of the microscopic processes underlying the temperature-dependent transport phenomena in p-doped GeSe and SnSe.

Our results predict a very high figure of merit for both out-of-plane (a-axis) and in-plane (c-axis) GeSe in a broad range of temperatures. This can be attributed to several factors that synergistically influence the performance: high Seebeck coefficients, extremely low Lorenz numbers, low hole thermal conductivities, very low lattice thermal conductivity, and a relatively large band gap. In fact, for temperatures above 500 K, out-of-plane GeSe is predicted to potentially have a higher zT than the record-breaking SnSe. By extending the analysis to 900 K, we obtain the outstanding zT values of 3.2 and 2.8 for the out-of-plane and in-plane directions with optimal carrier densities of 4×10^{19} and 5×10^{19} cm^{-3}, respectively. We find that the total relaxation time for the out-of-plane direction in GeSe is much higher than the corresponding relaxation time in SnSe, demonstrating the importance of directly calculating the relaxation times for GeSe.

II. THEORETICAL APPROACH

Hole-phonon (h-p) coupling and the scattering of holes by ionized impurities are the microscopic processes that determine the temperature-dependent p-type transport phenomena in TE materials, such as GeSe and SnSe. We calculate these TE transport properties from first-principles using the many-body perturbation theory of the h-p interaction following the Fan-Migdal approach and the Boltzmann transport formalism. The comprehensive theoretical framework for the calculation of the band-resolved (n) and momentum-resolved ($\mathbf{k}$) relaxation time (RT), $\tau_{n,\mathbf{k}}$, is described in detail in our previous work [28] and summarized in the supplemental material (SM) [53] for easy reference. In brief, we calculate three contributions to the total relaxation time. The nonpolar RT ($\tau_{\rm npol}$) comes from the short-range portion of the hole coupling to acoustic and optical phonons, which can be calculated using dual interpolation. The long-range portion of the hole coupling with optical phonons gives rise to the polar RT ($\tau_{\rm pol}$), which we determine using the analytic Vogl formula [54–56] with the addition of Ehrenreich screening [57]. Finally, extrinsic scattering by ionized impurities ($\tau_{\rm imp}$) is calculated using the theory developed by Brooks and Herring (BH) [58,59], which has been extended to go beyond the parabolic band approximation [60].

Assuming these scattering mechanisms can be treated independently, the total RT is determined by Mathiessen's rule, where the dependence of scattering times on independent variables, including temperature (T) and chemical potential (μ), is shown explicitly:

$$\frac{1}{\tau_{\rm tot}(n,\mathbf{k},\mu,T)} = \frac{1}{\tau_{\rm npol}(n,\mathbf{k},T)} + \frac{1}{\tau_{\rm pol}(n,\mathbf{k},\mu,T)} + \frac{1}{\tau_{\rm imp}(n,\mathbf{k},\mu,T)}. \qquad (1)$$

From $\tau_{\rm tot}$ we calculate the TE transport coefficients using the semiclassical BTE with the (nonconstant) relaxation time approximation (RTA) [60,61]. The key quantity is the momentum- and band-resolved transport distribution kernel,

$$\Sigma_{\alpha,\beta}(n,\mathbf{k},\mu,T) = e^2\tau_{n,\mathbf{k}}(\mu,T)v_\alpha(n,\mathbf{k})v_\beta(n,\mathbf{k}), \qquad (2)$$

where $\tau_{n,\mathbf{k}}(\mu,T) \equiv \tau_{\rm tot}$ is the total relaxation time, and $v(n,\mathbf{k})$ is the average group velocity. The energy-projected transport function can then be defined as

$$\Sigma_{\alpha,\beta}(\epsilon,\mu,T) = \frac{1}{N_{\mathbf{k}}}\sum_{\mathbf{k}}\Sigma_{\alpha,\beta}(n,\mathbf{k},\mu,T)\frac{\delta(\epsilon-\epsilon_{n,\mathbf{k}})}{d\epsilon}, \qquad (3)$$

and it is used to calculated the transport tensors in terms of the different energy moments

$$I^{(n)}_{\alpha,\beta}(T,\mu) = \frac{1}{\Omega}\int \Sigma_{\alpha,\beta}(\epsilon,\mu,T)(\epsilon-\mu)^n\left(-\frac{\partial f_\mu(\epsilon,T)}{\partial\epsilon}\right)d\epsilon. \qquad (4)$$

With the experimental conditions of zero temperature gradient ($\mathbf{\nabla}T = \mathbf{0}$) and zero electric current, the transport tensors yield the electrical conductivity,

$$\sigma \equiv \sigma_{\alpha,\beta}(T,\mu) = I^{(0)}_{\alpha,\beta}(T,\mu), \qquad (5)$$

the Seebeck coefficient,

$$S \equiv S_{i,j}(T,\mu) = (eT)^{-1}I^{(1)}_{\alpha,i}(T,\mu)/I^{(0)}_{\alpha,j}(T,\mu), \qquad (6)$$

and the charge carrier contribution to the thermal conductivity,

$$\kappa_{\mathrm{h}} \equiv \kappa^{h}_{i,j}(T,\mu) = (e^2T)^{-1}\big(I^{(2)}_{i,j}(T,\mu) - I^{(1)}_{i,\alpha}(T,\mu)I^{(0)}_{\beta,\alpha}(T,\mu)^{-1}I^{(1)}_{\beta,j}(T,\mu)\big). \quad (7)$$

III. COMPUTATIONAL DETAILS

Below are the details for calculations involving GeSe; the details for SnSe can be found in Ref. [28]. The relaxed geometry and electronic structure of GeSe were calculated using DFT, while the phonon dispersions and h-p matrix elements were calculated using DFPT, both implemented in the QUANTUM ESPRESSO package [62]. We employed fully relativistic optimized norm-conserving Vanderbilt pseudopotentials [63,64] within the generalized gradient approximation (GGA) for the exchange-correlation functional according to the formulation of Perdew-Burke-Ernzerhof (PBE) [65]. Monkhorst-Pack grids of 6 × 18 × 14 for **k**-point sampling and a kinetic energy cutoff of 80 Ry were employed to ensure the convergence of the total energy in DFT calculations. The energy convergence threshold for the total energy difference between two successive self-consistency steps was 10^{-11} Ry under the Davidson-type diagonalization method. Because DFT-GGA calculations underestimate the GeSe band gap, a scissor operator was used to rigidly shift the conduction bands upward in order to attain the experimental band gap of 1.1 eV [66,67].

At room temperature both GeSe and SnSe crystallize in a layered orthorhombic structure with the *Pnma* space group and eight atoms in the unit cell, shown in Fig. 1. The melting point of GeSe occurs at 948 ± 2 K [68–70], but according to Wiedemeier *et al.* [71], at 924 K a structural transition takes place from the orthorhombic phase to the ideal structure of NaCl type. This is controversial since according to Sist *et al.* [72], this structural phase transition occurs at the lower temperature of 907 K. For SnSe, a second-order phase transition to the higher symmetry *Cmcm* phase occurs at $T \sim 810$ K [73]. In the present work, we consider only *Pnma* orthorhombic structures for both materials, and thus we report their transport properties for temperatures up to 807 and 900 K for SnSe and GeSe, respectively.

Both materials form covalently bonded layers with zigzag chains along the b-axis and significant corrugation along the c-axis. Those layers are held together by much weaker van der Waals interactions along the out-of-plane a-axis. To capture such weak bonds between layers, we employed van der Waals corrections to DFT according to the D3 approach of Grimme *et al.* [74]. For GeSe, we started from the *Pnma* orthorhombic configuration from the Materials Project [75] (mp-700), and we relaxed the lattice parameters and atomic positions until all atomic force components were smaller in magnitude than 1 meV/Å. The relaxed lattice constants are $a = 11.02$ Å, $b = 3.58$ Å, and $c = 4.79$ Å, which are in reasonable agreement with the corresponding experimental values [71,76]. Importantly, our DFT-D3 calculations accurately reproduce the out-of-plane lattice constant (a-axis), differing from the experimental result at 919 K by only ∼0.1% [71].

We used our Turbo-EPW implementation [49] to calculate the RTs limited by h-p coupling, including both contributions of nonpolar and screened polar scatterings. Turbo-EPW takes advantage of the dual interpolation technique based on a first Wannier-Fourier interpolation [77,78], followed by a second interpolation using symmetry-adapted star functions, which allows for efficient interpolation of h-p scattering matrix elements onto dense meshes of electron (**k**) and phonon (**q**) wave vectors. In the present case, the first interpolation, using maximally localized Wannier functions determined by WANNIER90 [79], leads to a phonon grid of 10 × 40 × 20 **q** points. The calculated electron self-energy only changes by ∼2% for a ninefold denser **q** grid, indicating that our momentum sampling gives a well-converged balance between accuracy and computational cost. Subsequently, $M = 10$ star functions per **k** point were used for the second interpolation, resulting in a denser grid of 27 × 81 × 64 **k** points. In total, this results in over 1 billion **k**/**q** pairs.

The calculation of τ_{imp} requires static and high-frequency dielectric constants, ζ_0 and ζ_∞. We have used the experimental values [80,81] $\zeta_0 = 21.9, 30.4, 25.8$ (45, 62, 42) and $\zeta_\infty = 18.7, 21.9, 14.4$ (13, 17, 16) for the a-, b- and c-axis of GeSe (SnSe), respectively. We used the same value of $M = 10$ star functions in the calculation of τ_{imp} in order to obtain the same mesh for integration as in h-p calculations. Mathiessen's rule, Eq. (1), yields the temperature- and energy-dependent τ_{tot} that is used in our modified BOLTZTRAP code [60,61] to carry out transport calculations and determine all the TE properties.

IV. RESULTS AND DISCUSSION

A. Carrier density and ionized impurities concentration

The thermoelectric (TE) transport properties of GeSe depend on the carrier density, n_{carr}, and the concentration of ionized impurities, n_{ii}, both of which depend on the nonequilibrium growth process and can vary between samples. To make meaningful predictions, we need to determine experimentally relevant values for n_{carr} and n_{ii}, including realistic temperature evolution. Due to the structural and chemical similarities between GeSe and SnSe, and the dearth of experimental data on GeSe, we use the carrier and impurity concentrations derived from SnSe experiments as a reasonable estimate for the values in GeSe samples. This has the added benefit of allowing direct comparison of TE properties of two materials that differ only in chemical composition.

Following the same procedure used in Ref. [60], we determine n_{carr} and n_{ii} by self-consistently adjusting their values in order to reproduce, within our computational framework, the experimentally measured values of S and σ in p-doped SnSe reported by Zhao *et al.* [14]. Even though the carrier density of SnSe presents only weak anisotropy, as inferred by Hall measurements on SnSe [13], we considered different n_{carr} for the in-plane and the out-of-plane axes. We used the same temperature-dependent n_{carr} and n_{ii} derived for p-doped SnSe to calculate TE transport properties of p-doped GeSe. For reasons of clarity, in the main text we report the results for a- and b-axis p-doped GeSe (referred to in the following as a-GeSe and b-GeSe, respectively) using n_{carr} and n_{ii} derived from a-axis p-doped SnSe. Results for c-axis GeSe (c-GeSe),

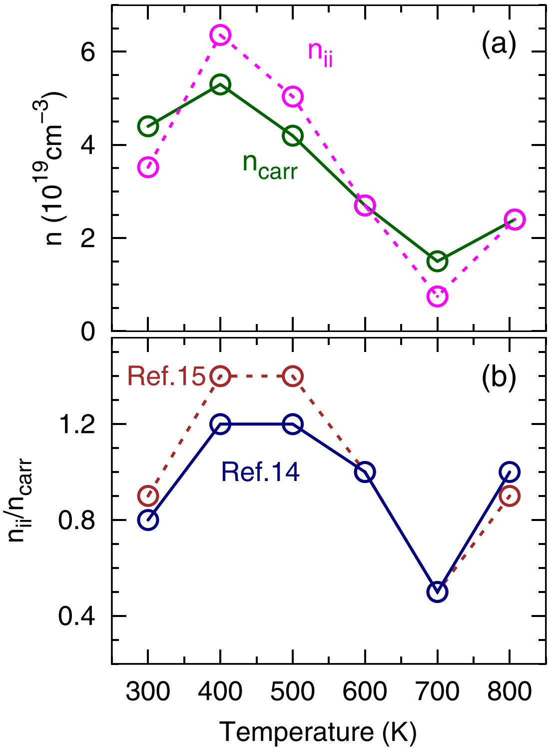

FIG. 2. (a) Carrier density, n_{carr} (green solid line), and ionized impurity concentration, n_{ii} (dashed magenta line), determined by self-consistently matching calculations to the experimental results for *a*-axis *p*-doped SnSe reported in Zhao *et al.* [14]. (b) The ratio of values in (a), $n_{\text{ii}}/n_{\text{carr}}$ (blue solid line), along with the same ratio as calculated in our previous work (brown dashed line) [28], derived from experimental results reported in Chang *et al.* [15] for the same axis.

as well as the properties calculated with n_{carr} and n_{ii} derived from *b*- or *c*-axis SnSe, are shown in Figs. S1–S3. For reasons of expedience, we approximated n_{carr} and n_{ii} of GeSe at 800 K by the values obtained at 807 K for SnSe.

Figure 2(a) shows the carrier and impurity concentrations derived for *a*-axis *p*-doped SnSe as a function of T. The results derived for *b*- and *c*-axis *p*-doped SnSe are shown in the SM [53] (Fig. S4). At 300 K, n_{carr} is approximately $4.4 \times 10^{19}\ \text{cm}^{-3}$, increases to $5.3 \times 10^{19}\ \text{cm}^{-3}$ at 400 K, and then decreases almost linearly down to $1.5 \times 10^{19}\ \text{cm}^{-3}$ at 700 K, all consistent with Hall measurements [14]. Above 700 K, our results indicate that n_{carr} increases due to vacancy formation [28], reaching $2.4 \times 10^{19}\ \text{cm}^{-3}$ at 807 K. Figure 2(b) shows the temperature dependence of the ratio $n_{\text{ii}}/n_{\text{carr}}$ compared to a previous calculation of the same quantity [28] that was based on the experimental data reported by Chang *et al.* [15] for a different *a*-axis SnSe sample with the same dopant. The similarity between the ratios determined in this work and those reported in our previous work demonstrates that these values of carrier and impurity concentrations are experimentally relevant and approximately sample-independent.

B. Thermoelectric transport properties

The calculated TE properties for *p*-doped out-of-plane (*a*-axis) and in-plane (*b*-axis) GeSe and SnSe are shown in Fig. 3, along with available experimental data [14]. All four systems show similar behavior of their Seebeck coefficients as a function of temperature, with S increasing with T up to 700 K, reaching 332 μV/K (326 μV/K) for *a*-GeSe (*b*-GeSe). Above that temperature, the increase in n_{carr} causes S to decrease to 319 μV/K (311 μV/K) at 800 K. For temperatures above 600 K, the calculated GeSe Seebeck coefficients are slightly higher than those of SnSe, in close agreement with previous theoretical findings [46,47]. As pointed out by Hao *et al.* [47],

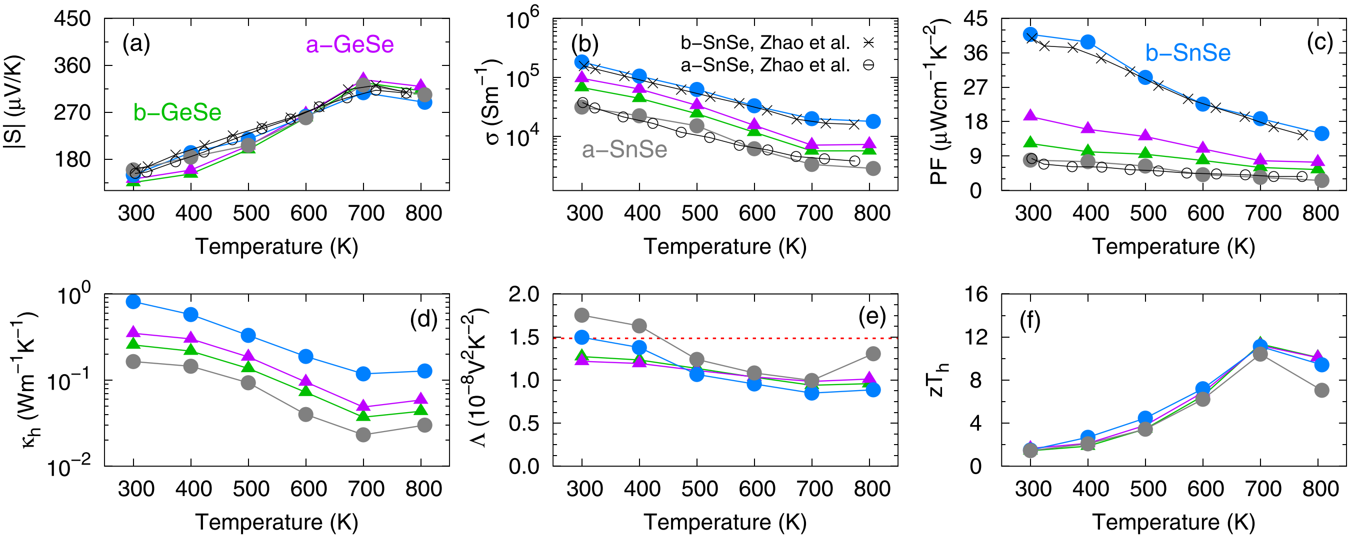

FIG. 3. Calculated TE transport properties of *p*-doped GeSe and SnSe as functions of temperature, along with available experimental data on *p*-doped SnSe reported by Zhao *et al.* [14]. (a) Seebeck coefficient, S; (b) electrical conductivity, σ; (c) power factor, PF; (d) thermal conductivity due to the hole transport, κ_{h}; (e) Lorenz function, Λ, with a dashed red line at Λ_{nd} (see the text); and (f) the hole figure of merit, zT_{h}.

p-doping in both materials induces a multiband effect that leads to an enhancement of S.

The electrical conductivity, σ, of all four systems shows the expected exponential decrease with temperature to 700 K, remaining nearly constant up to ∼800 K. Both axes of GeSe present σ values that are intermediate to those of a- and b-SnSe. As has been found previously, the in-plane electrical conductivity of GeSe is much lower than that of SnSe [47]. However, the out-of-plane σ of GeSe is greater than its in-plane σ and much higher than the out-of-plane conductivity in SnSe. This is a direct consequence of the low scattering rate by ionized impurities for holes close to the valence-band maximum (VBM) of a-GeSe, as will be discussed further below.

Similarly, the thermal conductivity due to hole transport, κ_{h}, also decreases with temperature up to 700 K and increases again for both materials between 700 and 800 K. The Lorenz function, defined as $\Lambda = \kappa_{\mathrm{h}}/(\sigma T)$, is shown in Fig. 3(e), along with a red dashed line at the nondegenerate limit for semiconductors, $\Lambda_{\mathrm{nd}} = 2(k_B/e)^2 = 1.485 \times 10^{-8}\ \mathrm{V}^2\,\mathrm{K}^{-2}$. It has been shown previously that Λ can be much smaller than Λ_{nd} when a rigorous first-principles approach is used instead of simplified band structures and scattering processes [82,83]. Additionally, even for simplified bands, Thesberg *et al.* [84] have shown that Λ can deviate markedly from Λ_{nd} due to multiband effects even if there is no explicit interband scattering. Both axes of GeSe have very small values of Λ that remain below Λ_{nd} throughout the temperature range. The Lorenz function for in-plane SnSe shows higher (lower) values than both axes of GeSe for temperatures below (above) 500 K. Even though a-SnSe also presents very low values of Λ, it is the highest of the four systems studied. Furthermore, it shows an abrupt enhancement above 700 K that is caused by a slight decrease in σ accompanied by a considerable increase in κ_{h}. Finally, the hole thermoelectric figure of merit, $zT_{\mathrm{h}} = S^2/\Lambda$, is shown in Fig. 3(f). zT_{h} values are quite similar for both materials throughout the entire temperature range, except for a-SnSe, which exhibits a sharp decrease at 800 K mirroring the increase in Λ.

C. Dominant scattering mechanisms and relaxation times

To understand the temperature-dependent transport phenomena in GeSe and SnSe, we extensively analyzed their carrier scattering mechanisms. Figure 4 shows the relaxation times (RTs) at 300 K due to nonpolar (τ_{npol}) and screened Fröhlich polar (τ_{pol}) scattering arising from the hole-phonon coupling, as well as scattering by ionized impurities (τ_{imp}) and the total RT (τ_{tot}) based on Mathiessen's rule, Eq. (1). These RTs are calculated as a function of the hole band and momentum, but plotted as a function of the hole energy using the following conversion:

$$\tau(\epsilon) = \frac{\sum_{n,\mathbf{k}} \tau_{n,\mathbf{k}} v_{n,\mathbf{k}} v_{n,\mathbf{k}} \delta(\epsilon - \epsilon_{n,\mathbf{k}})}{\sum_{n,\mathbf{k}} v_{n,\mathbf{k}} v_{n,\mathbf{k}} \delta(\epsilon - \epsilon_{n,\mathbf{k}})}. \qquad (8)$$

In the SM [53], we provide additional details about the temperature dependence of the RTs as well as comparisons between the RTs for different systems and axes.

Due to the effectiveness of screening in these doped systems, τ_{pol} is by far the largest RT, demonstrating that the Fröhlich coupling does not contribute significantly to the transport properties along either axis of p-doped GeSe. For both axes of GeSe we observe that τ_{imp} is competitive with τ_{npol} near the VBM at $E = 0$. For energies well below the VBM, τ_{imp} is quickly overtaken by τ_{npol}. Comparing the results for the two axes in GeSe, we observe that the total RTs are quite similar in magnitude and present similar energetic behavior, as can also be clearly seen in Fig. S5.

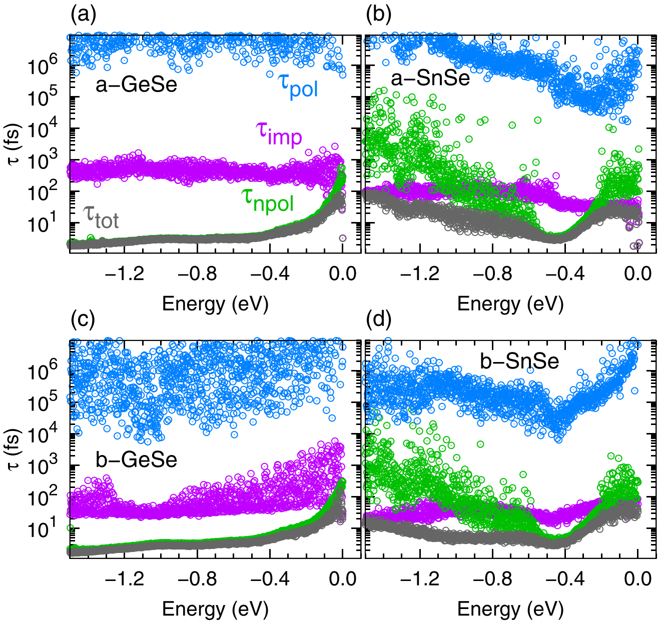

FIG. 4. Relaxation times (RTs) at 300 K as a function of hole energy for (a) p-doped GeSe (a-axis), (b) p-doped SnSe (a-axis), (c) p-doped GeSe (b-axis), and (d) p-doped SnSe (b-axis). Each panel includes the screened Fröhlich polar scattering of optical phonons (τ_{pol}, blue), nonpolar scattering of acoustic and optical phonons (τ_{npol}, green), scattering by ionized impurities (τ_{imp}, purple), and the total RT calculated with Mathiessen's rule (τ_{tot}, gray). The zero of the energy scale corresponds to the VBM.

For SnSe the scenario is more complex because τ_{npol} exhibits a nonmonotonic dependence on the hole energy with a minimum around $E = -0.5$ eV. In this case, τ_{imp} dominates the carrier scattering near the VBM for a-SnSe, while for b-SnSe, τ_{npol} and τ_{imp} compete with each other. τ_{npol} becomes dominant in the range of $E = -0.8$ to -0.2 eV, and the two mechanisms are comparable for lower energies. This complicated energy dependence of the RTs strongly affects the TE transport properties. In particular, it is responsible for the increase of κ_{h} at 807 K for a-SnSe, since the enhancement of τ_{npol} and greater importance of scattering at higher energies increases the integral that appears in the calculation of κ_{h} [28]. A detailed comparison between the RTs for both axes in p-doped SnSe is presented in the SM [53] (Figs. S6, S7, S8, and S9), demonstrating that near the VBM τ_{tot} is largely determined by τ_{imp}. Thus, it is the higher τ_{imp} that causes b-SnSe to have a larger τ_{tot} than a-SnSe throughout the full range of temperatures studied.

By carefully comparing the total RTs of both materials, we observe that GeSe presents higher RT close to the VBM, which can be attributed mainly to the weaker scattering of

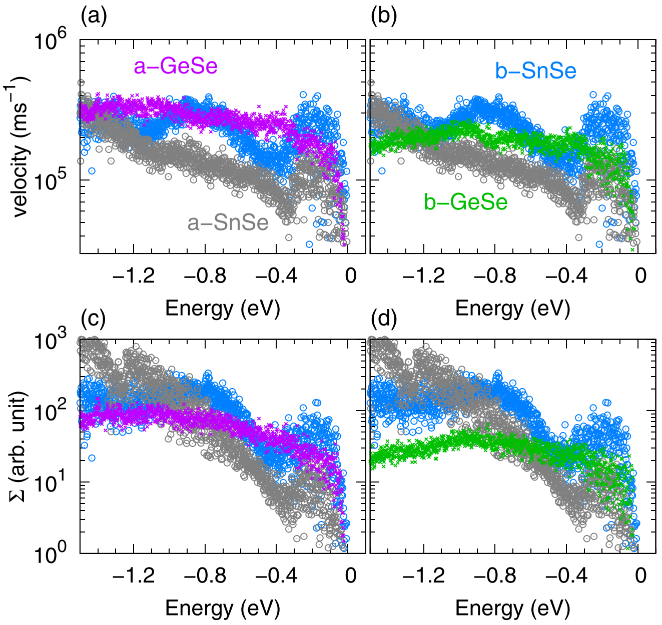

FIG. 5. Average hole group velocity as a function of hole energy for (a) GeSe (*a*-axis, purple) and (b) GeSe (*b*-axis, green). Transport distribution function Σ at 300 K as a function of hole energy for (c) GeSe (*a*-axis, purple) and (d) GeSe (*b*-axis, green). For comparison, each panel shows the values for SnSe, *a*-axis (gray) and *b*-axis (blue).

holes by ionized impurities (see Figs. S6 and S10). Since all other contributions to τ_{imp} are comparable in size, it must be the screening function F_{imp} that appears in the denominator of Eq. (S8) that leads to the larger RT. Hence, it is the greater effectiveness of the screening that raises the RT for GeSe. On the basis of Figs. S10–S13, the use of SnSe RTs to estimate the thermoelectric figure of merit for GeSe cannot be justified, since we see that the SnSe RTs are generally smaller near the VBM. Figure S11 clearly shows that such an approximation would significantly underestimate the RT for *a*-GeSe. In addition, the clear variations in RT with hole energy are a strong argument against the use of the constant relaxation-time approximation, which is in line with recent investigations on many materials [85,86].

D. Average hole group velocities and transport distribution function

The average hole group velocities as a function of energy can be derived from the calculated band structure:

$$v(\epsilon) = \sqrt{\sum_{n,\mathbf{k}} \left|\frac{\partial \epsilon_{n,\mathbf{k}}}{\partial \mathbf{k}}\right|^2 \delta(\epsilon - \epsilon_{n,\mathbf{k}}) \Bigg/ \sum_{n,\mathbf{k}} \delta(\epsilon - \epsilon_{n,\mathbf{k}})}. \qquad (9)$$

The group velocities, together with the energy-dependent transport distribution function, $\Sigma(\epsilon)$, are shown in Fig. 5 for in-plane and out-of-plane GeSe and SnSe. Clearly, *b*-SnSe has the highest velocities around the VBM, resulting in high electrical conductivity. Along the same lines, the lowest velocities in *a*-SnSe are responsible for its inferior overall TE properties. Close to the VBM, GeSe presents intermediate values for $v(\epsilon)$ and $\Sigma(\epsilon)$, higher than *a*-SnSe and lower than *b*-SnSe. Since the Seebeck coefficients of *a*-GeSe and *b*-GeSe are similar, it is the higher hole velocity, which leads to higher electrical conductivity, that results in the larger PF for *a*-GeSe. For GeSe, the velocities smoothly increase as hole energy increases away from the VBM, except for highly energetic holes in *b*-GeSe. On the other hand, for *b*-SnSe the velocities are high at the VBM, but they decrease with hole energy, becoming smaller than those of GeSe for holes between −0.3 and −0.6 eV. For GeSe, higher velocities at high hole energies contribute to the increase of κ_{h} between 700 and 800 K. In general, the behavior of $\Sigma(\epsilon)$ follows that of the velocities.

E. Outstanding thermoelectric performance of GeSe

To calculate the TE figure of merit, zT, we need an estimate of the total thermal conductivity, κ_{tot}. For SnSe, we use the experimental values measured by Zhao *et al.* [14]. Since the necessary measurements have not yet been made for GeSe, we rely on theoretical results based on the Debye-Callaway theory for lattice thermal conductivity [47], to which we add our calculated hole thermal conductivities. The resulting total thermal conductivity for both SnSe and GeSe is plotted in Fig. S14. The thermal conductivity is nearly the same for *a*-axis GeSe and SnSe, though at the highest temperatures it is slightly lower for *a*-GeSe. In-plane *b*-GeSe exhibits higher total thermal conductivity than out-of-plane GeSe throughout the temperature range, but it is comparatively lower than *b*-SnSe.

Both contributions to the total thermal conductivity are extremely low in GeSe. First, due to the relatively low electrical conductivity in GeSe and extremely low Lorenz numbers, carrier thermal conductivity is also very small. Second, GeSe displays strong anharmonicity as quantified by its large Grüneisen parameters, which are comparable to or even larger than the Grüneisen parameters for SnSe [47]. Such anomalously high Grüneisen parameters of GeSe are a consequence of its hingelike structure, distorted GeSe polyhedral, and van der Waals gaps in the out-of-plane direction that efficiently scatter phonons. Since the measured κ_{tot} for SnSe is extremely low, we expect the lattice contribution, κ_{latt}, to be extremely low for GeSe also.

In view of its relatively high Seebeck coefficients and extremely low Lorenz numbers, coupled with an ultralow κ_{tot}, we predict an outstanding TE performance for out-of-plane GeSe, as can be seen in Fig. 6. In particular, *a*-GeSe has zT values that equal or even exceed the record-breaking performance of *b*-SnSe at temperatures above 500 K. This result would be missed if we assumed that the RTs for GeSe were the same as those for SnSe along the corresponding crystallographic axis. Along with *a*-GeSe, high TE performance has also been obtained for *c*-GeSe throughout the whole temperature range, while *b*-GeSe has comparatively lower TE performance. It is important to emphasize that GeSe, just like SnSe, presents high zT over a wide temperature range, which is a consequence of its relatively large band gap [87]. Furthermore, we continue to find a high figure of merit for out-of-plane GeSe when using n_{carr} and n_{ii} derived from *b*- and *c*-SnSe data (see Figs. S15 and S16).

The figure of merit is increased for high power factors and low thermal conductivities. It is instructive to compare these

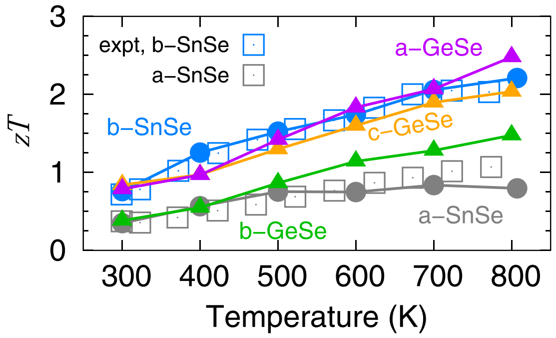

FIG. 6. Thermoelectric figure of merit (zT) as a function of temperature for p-doped a-GeSe (magenta), b-GeSe (green), c-GeSe (orange), a-SnSe (gray), and b-SnSe (blue). The experimental data reported by Zhao *et al.* [14] for both axes of p-doped SnSe are shown for comparison.

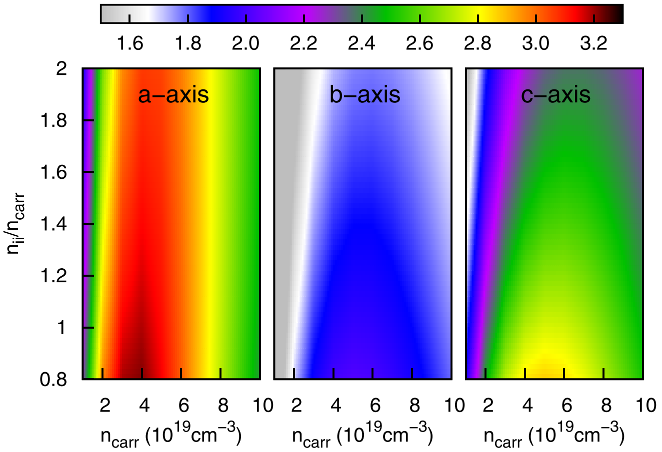

FIG. 7. Colormap of the thermoelectric performance figure of merit zT as a function of the variation in $n_{\rm carr}$ and in the ratio $n_{\rm ii}/n_{\rm carr}$ for out-of-plane (a-axis) and in-plane (b- and c-axis) GeSe at 900 K.

contributions to zT for each of the systems studied here. For SnSe, the out-of-plane direction has a low power factor and a low thermal conductivity, and the former dominates, leading to a (relatively) low zT value. In contrast, the in-plane direction has a high power factor and a high thermal conductivity, and once again it is the power factor that dominates, this time yielding a high zT value. Compared to its SnSe counterpart, b-GeSe has a much lower power factor as well as a somewhat lower thermal conductivity, producing a comparably low zT value. The surprise, at least with reference to SnSe, is that a-GeSe maintains a very low $\kappa_{\rm latt}$ without the dramatic decrease in PF shown by a-SnSe.

It is important to note that the calculation of $\kappa_{\rm latt}$ is very challenging. For SnSe, there is a long debate about $\kappa_{\rm latt}$ in the experimental literature [88–91] as well as questions regarding the comparison with first-principles calculations [89]. Similarly, the intrinsic thermal conductivity of GeSe is likely to be the subject of intense debate. Therefore, we recalculated the value of zT for GeSe using values for $\kappa_{\rm latt}$ determined by Yuan *et al.* [92] based on third-order force constants. Their values of $\kappa_{\rm latt}$ are noticeably higher, leading to a lower prediction for zT as shown in the SM [53] (Fig. S17). Even with the larger $\kappa_{\rm latt}$, a-GeSe presents a reasonable TE performance, reaching $zT = 1.56$ at 800 K for $n_{\rm carr}$ and $n_{\rm ii}$ derived from a-SnSe. Though the approach of Yuan *et al.* [92] is more realistic than Debye-Callaway theory, the example of chalcogenides has shown that including additional factors such as thermal expansion, anharmonic phonon renormalization, four-phonon scattering, and impurity scatterings all generally serve to reduce the calculated values of $\kappa_{\rm latt}$ [89,93], bringing them closer to the simpler Debye-Callaway approximation. Since doped GeSe is a strongly anharmonic material, it is not unreasonable that the Debye-Callaway method might yield reasonable results, as it has for other low-conductivity thermoelectric compounds [94].

Since GeSe should maintain its *Pnma* structure at higher temperatures than SnSe, we extend our analysis to 900 K. At that high temperature, we estimate $\kappa_{\rm latt}$ using a $1/T$ extrapolation [95] of the theoretical calculations done by Hao *et al.* [47]. To that result we add κ_h calculated within our current framework. However, due to its phase transition, there are no SnSe transport data at 900 K that we can use to determine $n_{\rm carr}$ and $n_{\rm ii}$. Instead, we scan over a range of $n_{\rm carr}$ and the ratio $n_{\rm ii}/n_{\rm carr}$ and carry out transport calculations by solving the BTE for each pair of values. The density $n_{\rm carr}$ is varied between $1 \times 10^{19}\,{\rm cm}^{-3}$ and $10 \times 10^{19}\,{\rm cm}^{-3}$ in 10 equally spaced steps, while for each value of $n_{\rm carr}$, $n_{\rm ii}/n_{\rm carr}$ was varied between 0.8 to 2.0 in steps of 0.2.

The calculated zT values along all three crystallographic axes of GeSe at 900 K are shown as a function of $n_{\rm carr}$ and $n_{\rm ii}/n_{\rm carr}$ in Fig. 7. The out-of-plane direction presents the highest performance in comparison to the other axes, reaching the ultrahigh value of $zT = 3.2$ at optimal $n_{\rm carr} = n_{\rm ii} = 4 \times 10^{19}\,{\rm cm}^{-3}$. It is important to note that zT remains very high even if the ratio $n_{\rm ii}/n_{\rm carr}$ increases. For example, $zT = 3.06$ when $n_{\rm ii}/n_{\rm carr} = 2$, indicating a high performance with zT larger than 3 even if $n_{\rm ii}$ is doubled. Horizontal line cuts at fixed ratios are shown in Fig. S18, clearly demonstrating that a tenfold increase in the ratio $n_{\rm ii}/n_{\rm carr}$ can still lead to great performance provided $n_{\rm carr}$ is correspondingly increased. For example, with $n_{\rm ii}/n_{\rm carr} = 10$, an optimal value of $n_{\rm carr} = 6 \times 10^{19}\,{\rm cm}^{-3}$ yields $zT = 2.7$. Figure S18 also shows the robustness of the high zT values as $n_{\rm carr}$ is varied. For instance, $zT \geqslant 3$ for $n_{\rm carr}$ between $3 \times 10^{19}\,{\rm cm}^{-3}$ and $6 \times 10^{19}\,{\rm cm}^{-3}$ when $n_{\rm ii}/n_{\rm carr} = 1$. Though not as impressive as the out-of-plane direction, the two in-plane directions still exhibit relatively high zT values at 900 K, namely $zT = 2.0$ (2.8) for the optimal ratio $n_{\rm carr} = n_{\rm ii} = 5 \times 10^{19}\,{\rm cm}^{-3}$ for the b-axis (c-axis).

V. CONCLUSIONS

In summary, we applied extensive first-principles calculations within the BTE framework to thoroughly investigate the temperature dependence of the TE transport properties of the orthorhombic *Pnma* phase of p-doped GeSe and SnSe. These calculations were done for values of the carrier density that yielded the record-breaking TE performance of p-doped SnSe [14]. We explicitly calculated the RTs due to nonpolar and screened Fröhlich polar h-p scattering, as well as the RT associated with the scattering by ionized impurities. The obtained temperature and hole-energy dependent RTs provide insight into the microscopic origin of the transport properties in *p*-doped GeSe and SnSe.

Our results indicate that the calculated GeSe Seebeck coefficients, S, are slightly higher than those of SnSe at temperatures above 600 K, while both axes of GeSe present electrical conductivity values that are intermediate between those of *a*- and *b*-SnSe. Importantly, both axes of GeSe exhibit Lorenz numbers below the nondegenerate limit of semiconductors. In-plane SnSe also has very low values for the Lorenz function Λ, and at temperatures above 500 K they are the same as or even smaller than those of in-plane GeSe. On the other hand, *a*-SnSe possesses the highest Λ among all studied systems. Those results for Λ are directly correlated with TE performance, in which a low Λ plays a beneficial role in obtaining a high zT_{h}.

All axes of GeSe have quite low thermal conductivity κ_{tot}, which is a consequence of relatively low σ that yields low hole thermal conductivity, and high anharmonicity [47] that leads to predictions of low κ_{latt}. Combined with the high Seebeck coefficients, extremely low Lorenz numbers, and a relatively large band gap, our calculations predict an outstanding TE performance for both out-of-plane (*a*-axis) and in-plane (*b*- and *c*-axis) GeSe throughout a wide range of temperatures. Above 500 K, the out-of-plane direction has zT values equal to or greater than the record-breaking performance of *b*-SnSe. By extending the analysis of the TE performance of GeSe to 900 K, we find that the out-of-plane direction still presents the highest performance compared to other axes, reaching an ultrahigh $zT = 3.2$ at the optimal carrier density of 4×10^{19} cm^{-3}. In addition, the two in-plane axes also have impressive figures of merit, with $zT = 2.0$ (2.8) for the *b*-axis (*c*-axis) with an optimal carrier density of 5×10^{19} cm^{-3}. It is important to point out that the total RTs of out-of-plane GeSe are much higher than those of *a*-SnSe. Thus our results for the out-of-plane direction could not be anticipated by calculations using the same RTs as those for SnSe [47].

Finally, it is also important to point out that intrinsic GeSe possesses low carrier density. To date, Ge substitution by Ag is the most effective method of doping, enabling a hole density up to $\sim 10^{18}$ cm^{-3} and $zT \approx 0.2$ at 700 K for polycrystalline GeSe [48]. This experimental result is far below our highest theoretically predicted value of $zT = 3.2$ at 900 K, which can be attributed to the low carrier density that is far below our predicted optimal carrier density of $\sim 10^{19}$ cm^{-3}. Our results indicate that there is enormous room for further improvement in the TE performance of GeSe by increasing the doping to optimal carrier density.

All computer implementations of the methodology developed in this project were written in FORTRAN 90 and are available upon request.

ACKNOWLEDGMENTS

A.S.C. and A.A. gratefully acknowledge support from the Brazilian agencies CNPq and FAPESP under Grants No. 2010/16970-0, No. 2013/08293-7, No. 2015/26434-2, No. 2016/23891-6, No. 2017/26105-4, and No. 2019/26088-8. D.T.L. acknowledges funding from the STC Center for Integrated Quantum Materials, NSF Grant No. DMR-1231319; NSF DMREF Award No. 1922172; and the Army Research Office under Cooperative Agreement No. W911NF-21-2-0147. The calculations were performed at CCJDR-IFGW-UNICAMP in Brazil.

There are no conflicts to declare.

[1] J. Mao, G. Chen, and Z. Ren, Nat. Mater. **20**, 454 (2021).

[2] J. Mao, H. Zhu, Z. Ding, Z. Liu, G. A. Gamage, G. Chen, and Z. Ren, Science **365**, 495 (2019).

[3] F. J. DiSalvo, Science **285**, 703 (1999).

[4] J. He and T. M. Tritt, Science **357**, eaak9997 (2017).

[5] H. Lv, H. Liu, J. Shi, X. Tang, and C. Uher, J. Mater. Chem. A **1**, 6831 (2013).

[6] R. Venkatasubramanian, E. Siivola, T. Colpitts, and B. O'quinn, Nature **413**, 597 (2001).

[7] Y. Zhang, S. Hao, L.-D. Zhao, C. Wolverton, and Z. Zeng, J. Mater. Chem. A **4**, 12073 (2016).

[8] B. Zhong, Y. Zhang, W. Li, Z. Chen, J. Cui, W. Li, Y. Xie, Q. Hao, and Q. He, Appl. Phys. Lett. **105**, 123902 (2014).

[9] M. Famili, I. M. Grace, Q. Al-Galiby, H. Sadeghi, and C. J. Lambert, Adv. Funct. Mater. **28**, 1703135 (2018).

[10] Q. Xue, H. Liu, D. Fan, L. Cheng, B. Zhao, and J. Shi, Phys. Chem. Chem. Phys. **18**, 17912 (2016).

[11] H. Ohta, S. Kim, Y. Mune, T. Mizoguchi, K. Nomura, S. Ohta, T. Nomura, Y. Nakanishi, Y. Ikuhara, M. Hirano, H. Hosono, and K. Koumoto, Nat. Mater. **6**, 129 (2007).

[12] T. Fu, X. Yue, H. Wu, C. Fu, T. Zhu, X. Liu, L. Hu, P. Ying, J. He, and X. Zhao, J. Materiomics **2**, 141 (2016).

[13] L.-D. Zhao, S.-H. Lo, Y. Zhang, H. Sun, G. Tan, C. Uher, C. Wolverton, V. P. Dravid, and M. G. Kanatzidis, Nature **508**, 373 (2014).

[14] L.-D. Zhao, G. Tan, S. Hao, J. He, Y. Pei, H. Chi, H. Wang, S. Gong, H. Xu, V. P. Dravid, C. Uher, G. J. Snyder, C. Wolverton, and M. G. Kanatzidis, Science **351**, 141 (2016).

[15] C. Chang, M. Wu, D. He, Y. Pei, C.-F. Wu, X. Wu, H. Yu, F. Zhu, K. Wang, Y. Chen, L. Huang, J.-F. Li, J. He, and L.-D. Zhao, Science **360**, 778 (2018).

[16] C. B. Vining, Nat. Mater. **8**, 83 (2009).

[17] B. Sales, D. Mandrus, and R. K. Williams, Science **272**, 1325 (1996).

[18] C. Zhou, Y. K. Lee, Y. Yu, S. Byun, Z.-Z. Luo, H. Lee, B. Ge, Y.-L. Lee, X. Chen, J. Y. Lee, C.-M. Oana, H. Chang, J. Im, S.-P. Cho, M. Wuttig, V. P. Dravid, M. G. Kanatzidis, and I. Chung, Nat. Mater. **20**, 1378 (2021).

[19] Y. Pei, X. Shi, A. LaLonde, H. Wang, L. Chen, and G. J. Snyder, Nature **473**, 66 (2011).

[20] Y. Pei, H. Wang, and G. J. Snyder, Adv. Mater. **24**, 6125 (2012).

[21] A. M. Dehkordi, M. Zebarjadi, J. He, and T. M. Tritt, Mater. Sci. Eng.: R **97**, 1 (2015).

[22] L.-D. Zhao, S. Hao, S.-H. Lo, C.-I. Wu, X. Zhou, Y. Lee, H. Li, K. Biswas, T. P. Hogan, C. Uher, C. Wolverton, V. P. Dravid, and K. M. G, J. Am. Chem. Soc. **135**, 7364 (2013).

[23] W. Liu, X. Tan, K. Yin, H. Liu, X. Tang, J. Shi, Q. Zhang, and C. Uher, Phys. Rev. Lett. **108**, 166601 (2012).

[24] D. S. Parker, A. F. May, and D. J. Singh, Phys. Rev. Appl. **3**, 064003 (2015).
[25] X. Chen, D. Parker, and D. J. Singh, Sci. Rep. **3**, 3168 (2013).
[26] R. L. González-Romero, A. Antonelli, A. S. Chaves, and J. J. Meléndez, Phys. Chem. Chem. Phys. **20**, 1809 (2018).
[27] R. W. McKinney, P. Gorai, V. Stevanović, and E. S. Toberer, J. Mater. Chem. A **5**, 17302 (2017).
[28] A. S. Chaves, D. T. Larson, E. Kaxiras, and A. Antonelli, Phys. Rev. B **104**, 115204 (2021).
[29] A. I. Hochbaum, R. Chen, R. D. Delgado, W. Liang, E. C. Garnett, M. Najarian, A. Majumdar, and P. Yang, Nature **451**, 163 (2008).
[30] A. I. Boukai, Y. Bunimovich, J. Tahir-Kheli, J.-K. Yu, W. A. Goddard III, and J. R. Heath, Nature **451**, 168 (2008).
[31] M. G. Kanatzidis, Chem. Mater. **22**, 648 (2009).
[32] C. J. Vineis, A. Shakouri, A. Majumdar, and M. G. Kanatzidis, Adv. Mater. **22**, 3970 (2010).
[33] K. Biswas, J. He, I. D. Blum, C.-I. Wu, T. P. Hogan, D. N. Seidman, V. P. Dravid, and M. G. Kanatzidis, Nature **489**, 414 (2012).
[34] H. Liu, X. Shi, F. Xu, L. Zhang, W. Zhang, L. Chen, Q. Li, C. Uher, T. Day, and G. J. Snyder, Nat. Mater. **11**, 422 (2012).
[35] A. Olvera, N. Moroz, P. Sahoo, P. Ren, T. Bailey, A. Page, C. Uher, and P. Poudeu, Energy Environ. Sci. **10**, 1668 (2017).
[36] Y. Cheng, J. Yang, Q. Jiang, D. He, J. He, Y. Luo, D. Zhang, Z. Zhou, Y. Ren, and J. Xin, J. Mater. Chem. A **5**, 5163 (2017).
[37] N. Ma, Y.-Y. Li, L. Chen, and L.-M. Wu, J. Am. Chem. Soc. **142**, 5293 (2020).
[38] S. Roychowdhury, T. Ghosh, R. Arora, M. Samanta, L. Xie, N. K. Singh, A. Soni, J. He, U. V. Waghmare, and K. Biswas, Science **371**, 722 (2021).
[39] M. Taniguchi, R. Johnson, J. Ghijsen, and M. Cardona, Phys. Rev. B **42**, 3634 (1990).
[40] A. Okazaki, J. Phys. Soc. Jpn. **13**, 1151 (1958).
[41] P. D. Antunez, J. J. Buckley, and R. L. Brutchey, Nanoscale **3**, 2399 (2011).
[42] S.-C. Liu, Y. Mi, D.-J. Xue, Y.-X. Chen, C. He, X. Liu, J.-S. Hu, and L.-J. Wan, Adv. Electr. Mater. **3**, 1700141 (2017).
[43] Z. Huang, S. A. Miller, B. Ge, M. Yan, S. Anand, T. Wu, P. Nan, Y. Zhu, W. Zhuang, G. J. Snyder, P. Jiang, and X. Bao, Angewandte Chem. Int. Ed. **56**, 14113 (2017).
[44] D. Sarkar, T. Ghosh, S. Roychowdhury, R. Arora, S. Sajan, G. Sheet, U. V. Waghmare, and K. Biswas, J. Am. Chem. Soc. **142**, 12237 (2020).
[45] D. Sarkar, S. Roychowdhury, R. Arora, T. Ghosh, A. Vasdev, B. Joseph, G. Sheet, U. V. Waghmare, and K. Biswas, Angewand. Chem. **133**, 10438 (2021).
[46] G. Ding, G. Gao, and K. Yao, Sci. Rep. **5**, 1 (2015).
[47] S. Hao, F. Shi, V. P. Dravid, M. G. Kanatzidis, and C. Wolverton, Chem. Mater. **28**, 3218 (2016).
[48] X. Zhang, J. Shen, S. Lin, J. Li, Z. Chen, W. Li, and Y. Pei, J. Materiomics **2**, 331 (2016).
[49] A. S. Chaves, A. Antonelli, D. T. Larson, and E. Kaxiras, Phys. Rev. B **102**, 125116 (2020).
[50] P. Hohenberg and W. Kohn, Phys. Rev. **136**, B864 (1964).
[51] W. Kohn and L. J. Sham, Phys. Rev. **140**, A1133 (1965).
[52] S. Baroni, S. De Gironcoli, A. Dal Corso, and P. Giannozzi, Rev. Mod. Phys. **73**, 515 (2001).
[53] See Supplemental Material at http://link.aps.org/supplemental/10.1103/PhysRevB.105.205201. for a more comprehensive theoretical framework, additional details about the temperature dependence of the relaxation times (RTs), comparisons between the RTs for different systems and axes, additional analysis of the carrier densities, concentration of ionized impurities, and thermoelectric figure of merit for different axes and conditions. The supplemental material contains additional Refs. [96–104].
[54] C. Pellegrini, A. Marinelli, and S. Reiche, Rev. Mod. Phys. **88**, 015006 (2016).
[55] C. Bostedt, S. Boutet, D. M. Fritz, Z. Huang, H. J. Lee, H. T. Lemke, A. Robert, W. F. Schlotter, J. J. Turner, and G. J. Williams, Rev. Mod. Phys. **88**, 015007 (2016).
[56] P. Vogl, Phys. Rev. B **13**, 694 (1976).
[57] H. Ehrenreich, J. Phys. Chem. Solids **8**, 130 (1959).
[58] H. Brooks, in *Advances in Electronics and Electron Physics* (Elsevier, Amsterdam, 1955), Vol. 7, pp. 85–182.
[59] D. Chattopadhyay and H. Queisser, Rev. Mod. Phys. **53**, 745 (1981).
[60] A. S. Chaves, R. L. González-Romero, J. J. Meléndez, and A. Antonelli, Phys. Chem. Chem. Phys. **23**, 900 (2021).
[61] G. K. Madsen and D. J. Singh, Comput. Phys. Commun. **175**, 67 (2006).
[62] P. Giannozzi, S. Baroni, N. Bonini, M. Calandra, R. Car, C. Cavazzoni, D. Ceresoli, G. L. Chiarotti, M. Cococcioni, I. Dabo, A. Dal Corso, S. de Gironcoli, S. Fabris, G. Fratesi, R. Gebauer, U. Gerstmann, C. Gougoussis, A. Kokalj, M. Lazzeri, L. Martin-Samos, N. Marzari, F. Mauri, R. Mazzarello, S. Paolini, A. Pasquarello, L. Paulatto, C. Sbraccia, S. Scandolo, G. Sclauzero, A. P. Seitsonen, A. Smogunov, P. Umari, and R. M. Wentzcovitch, J. Phys.: Condens. Matter **21**, 395502 (2009).
[63] D. Hamann, Phys. Rev. B **88**, 085117 (2013).
[64] M. Van Setten, M. Giantomassi, E. Bousquet, M. J. Verstraete, D. R. Hamann, X. Gonze, and G.-M. Rignanese, Comput. Phys. Commun. **226**, 39 (2018).
[65] J. P. Perdew, K. Burke, and M. Ernzerhof, Phys. Rev. Lett. **77**, 3865 (1996).
[66] A. Elkorashy, Phys. Status Solidi B **152**, 249 (1989).
[67] D. D. Vaughn, R. J. Patel, M. A. Hickner, and R. E. Schaak, J. Am. Chem. Soc. **132**, 15170 (2010).
[68] L. Ross and M. Bourgon, Can. J. Chem. **47**, 2555 (1969).
[69] H. Ipser, M. Gambino, and W. Schuster, Monatsh. Chem./Chem. Monthly **113**, 389 (1982).
[70] D. Bletskan, J. Ovonic Res. **1**, 53 (2005).
[71] H. Wiedemeier and P. Siemers, Z. Anorg. Allgem. Chem. **411**, 90 (1975).
[72] M. Sist, C. Gatti, P. Nørby, S. Cenedese, H. Kasai, K. Kato, and B. B. Iversen, Chem.–A Eur. J. **23**, 6888 (2017).
[73] C. W. Li, J. Hong, A. F. May, D. Bansal, S. Chi, T. Hong, G. Ehlers, and O. Delaire, Nat. Phys. **11**, 1063 (2015).
[74] S. Grimme, J. Antony, S. Ehrlich, and H. Krieg, J. Chem. Phys. **132**, 154104 (2010).
[75] A. Jain, S. P. Ong, G. Hautier, W. Chen, W. D. Richards, S. Dacek, S. Cholia, D. Gunter, D. Skinner, G. Ceder, and K. A. Persson, APL Mater. **1**, 011002 (2013).
[76] H. Wiedemeier and H. G. von Schnering, Z. Kristallogr. **148**, 3 (1978).

[77] F. Giustino, M. L. Cohen, and S. G. Louie, Phys. Rev. B **76**, 165108 (2007).

[78] S. Poncé, E. R. Margine, C. Verdi, and F. Giustino, Comput. Phys. Commun. **209**, 116 (2016).

[79] A. A. Mostofi, J. R. Yates, Y.-S. Lee, I. Souza, D. Vanderbilt, and N. Marzari, Comput. Phys. Commun. **178**, 685 (2008).

[80] O. Madelung, *Semiconductors: Data Handbook* (Springer Science & Business Media, Berlin, Heidelberg, 2004).

[81] H. Chandrasekhar, R. Humphreys, U. Zwick, and M. Cardona, Phys. Rev. B **15**, 2177 (1977).

[82] X. Wang, V. Askarpour, J. Maassen, and M. Lundstrom, J. Appl. Phys. **123**, 055104 (2018).

[83] A. Putatunda and D. J. Singh, Mater. Today Phys. **8**, 49 (2019).

[84] M. Thesberg, H. Kosina, and N. Neophytou, Phys. Rev. B **95**, 125206 (2017).

[85] P. Graziosi, C. Kumarasinghe, and N. Neophytou, ACS Appl. Energy Mater. **3**, 5913 (2020)

[86] A. M. Ganose, J. Park, A. Faghaninia, R. Woods-Robinson, K. A. Persson, and A. Jain, Nat. Commun. **12**, 1 (2021).

[87] Y. Xiao and L.-D. Zhao, Science **367**, 1196 (2020).

[88] P.-C. Wei, S. Bhattacharya, J. He, S. Neeleshwar, R. Podila, Y. Chen, and A. Rao, Nature **539**, E1 (2016).

[89] D. Wu, L. Wu, D. He, L.-D. Zhao, W. Li, M. Wu, M. Jin, J. Xu, J. Jiang, L. Huang, Y. Zhu, M. G. Kanatzidis, and J. He, Nano Energy **35**, 321 (2017).

[90] G. Li, U. Aydemir, M. Wood, W. A. Goddard III, P. Zhai, Q. Zhang, and G. J. Snyder, Chem. Mater. **29**, 2382 (2017).

[91] Y.-X. Chen, Z.-H. Ge, M. Yin, D. Feng, X.-Q. Huang, W. Zhao, and J. He, Adv. Funct. Mater. **26**, 6836 (2016).

[92] K. Yuan, Z. Sun, X. Zhang, and D. Tang, Sci. Rep. **9**, 1 (2019).

[93] Y. Xia, Appl. Phys. Lett. **113**, 073901 (2018).

[94] Y. Zhang, E. Skoug, J. Cain, V. Ozoliņš, D. Morelli, and C. Wolverton, Phys. Rev. B **85**, 054306 (2012).

[95] G. Grimvall, *Thermophysical Properties of Materials* (Elsevier, Amsterdam, 1999).

[96] F. Giustino, Rev. Mod. Phys. **89**, 015003 (2017).

[97] S. Poncé, E. R. Margine, and F. Giustino, Phys. Rev. B **97**, 121201(R) (2018).

[98] S. Poncé, W. Li, S. Reichardt, and F. Giustino, Rep. Progr. Phys. **83**, 036501 (2020).

[99] H. Fröhlich, Proc. R. Soc. (London) **160**, 230 (1937).

[100] C. Verdi and F. Giustino, Phys. Rev. Lett. **115**, 176401 (2015).

[101] N. Marzari and D. Vanderbilt, Phys. Rev. B **56**, 12847 (1997).

[102] B. M. Askerov and S. Figarova, *Thermodynamics, Gibbs Method and Statistical Physics of Electron Gases* (Springer Science & Business Media, Berlin, Heidelberg, 2009), Vol. 57.

[103] D. G. Shankland, in *Computational Methods in Band Theory* (Plenum Press, New York, 1971), pp. 362–367.

[104] D. Koelling and J. Wood, J. Computat. Phys. **67**, 253 (1986).